

Identification of Recombination Losses in CdSe/CdTe Solar Cells from Spectroscopic and Microscopic Time-Resolved Photoluminescence

Darius Kuciauskas,* John Moseley, and Chungho Lee

Due to the lowest-cost and best reliability, CdTe solar cells are the leading thin-film photovoltaic technology. Increasing open-circuit voltage by reducing recombination represents the most promising path toward further improvements. Analysis is needed to identify limitations that cause efficiency losses. To achieve this goal for Cu-doped CdSe/CdTe solar cells, time-resolved spectroscopy and microscopy are developed and applied. Recombination lifetimes and radiative efficiency identify that defect-mediated recombination is the dominant voltage loss mechanism. When carrier lifetimes are averaged over many crystalline grains, they increase from 180 to 430 ns when Al_2O_3 is applied to the back contact. The quasi-Fermi-level splitting correspondingly increases from 880–905 to 906–931 mV, indicating a pathway to overcome the long-standing 900 mV voltage limitation. However, the dominant recombination losses are attributed to the absorber bulk. From microscopic carrier lifetime measurements, it is identified that space charge fields due to charged grain boundaries (GBs) lead to recombination in the CdTe absorber bulk. At high injection, GB space charge fields are screened, but that occurs above 1 Sun excitation conditions. Alloying with selenium in the near-interface CdSeTe absorber region reduces GB losses and is identified as one of the factors leading to high radiative and power conversion efficiency.

1. Introduction

As a result of exponential growth, thin-film photovoltaics (PVs) are annually deployed on the 10 GW scale. However, cumulative tens-of-TW PV installations are envisioned^[1] and PV materials and devices need to be improved considerably to enable such

progress. Higher solar cell efficiency is the primary driver of PV growth, as it reduces PV costs and allows it to compete with other energy technologies, thus increasing carbon-free energy resource.^[1] Pathways to higher solar cell efficiency benchmarked in modeling studies include reducing Shockley–Read–Hall (SRH) recombination and increasing doping, both of which increase quasi-Fermi-level splitting (qFLS) in the semiconductor absorber.^[2–5]


In this study, we analyze Cu-doped bilayer CdSe/CdTe solar cells (Figure 1). First Solar annually produces about 6 GW of such solar cells, which makes them leading thin-film PV technology. In addition, Cu(In,Ga)Se₂ thin-film solar cells are annually installed on 2 GW scale, and perovskite PVs is actively investigated for future applications. For CdTe, power conversion efficiency reached 22.1% (open-circuit voltage $V_{\text{OC}} = 887$ mV) for small area cells^[6] and 19.0% for large area (>2 m²) commercial modules.^[7] The Shockley–Queisser (SQ) voltage for CdSeTe bandgap of $E_g = 1.42$ eV is $V_{\text{OC,SQ}} = 1.157$ V.^[8] Since CdSe/CdTe solar cells achieved only 77% SQ voltage, reducing recombination affords considerable opportunity to increase voltage and efficiency. This is especially important for CdTe PV, because some other solar cells (e.g., silicon, perovskites) have achieved >85% SQ V_{OC} .^[8,9] Using a model system where back contact is passivated with Al_2O_3 , we identify that passivating back contact can allow higher qFLS, thus overcoming longstanding 900 mV qFLS barrier. However, we show that the dominant recombination losses occur in the bulk of the absorber.

To characterize losses in CdTe solar cells, electrical or optical methods are typically used.^[10] In this study, analysis is based on carrier lifetime measurements. Carrier lifetimes are usually measured after pulsed laser excitation by recording band edge radiative emission with time-resolved photoluminescence (TRPL), and TRPL data have shown correlations between lifetime τ_{TRPL} and V_{OC} in thin-film solar cells.^[11–13] We update this analysis for CdSe/CdTe solar cells with increased carrier lifetimes by estimating qFLS and radiative efficiency from the lifetime data.

When recombination lifetimes are measured microscopically with a focused laser beam, measurements offer opportunity to analyze spatial distributions of recombination locations, which in polycrystalline films can include grain boundaries (GBs).^[14–16]

Dr. D. Kuciauskas, Dr. J. Moseley
Materials, Chemical, and Computational Sciences
National Renewable Energy Laboratory
15013 Denver West Parkway, Golden, CO 80401, USA
E-mail: Darius.Kuciauskas@nrel.gov

Dr. C. Lee
California Advanced Research
First Solar
1035 Walsh Avenue, Santa Clara, CA 95050, USA

 The ORCID identification number(s) for the author(s) of this article can be found under <https://doi.org/10.1002/solr.202000775>.

The publisher acknowledges that the United States Government retains a non-exclusive, paid-up, irrevocable, world-wide license to publish or reproduce the published form of this article, or allow others to do so, for United States Government purposes only.

DOI: 10.1002/solr.202000775

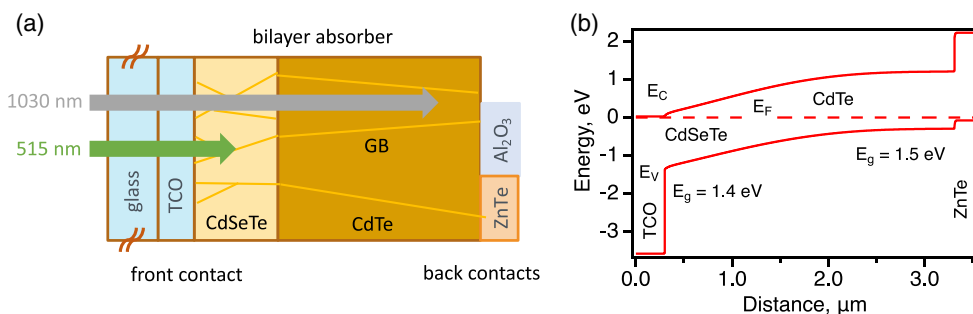


Figure 1. a) Illustration of Cu-doped CdSe/CdTe thin-film solar cell. ZnTe contact is used in devices, Al_2O_3 was used for passivation. GB is grain boundary, TCO is transparent conductive oxide (SnO_2). b) Band diagram for ZnTe back contact devices. E_C is energy of the conduction band, E_V is energy of the valence band, E_g is bandgap, and E_F is Fermi energy.

When carrier diffusion length exceeds dimensions of the focused laser beam, carrier dynamics can also be impacted by the lateral drift and diffusion.^[17–20] As a result, currently there are no accepted analytical methods for microscopic carrier lifetime analysis in solar cells.^[19] Here, we apply spectroscopic and microscopic measurements to the same samples and establish conditions when microscopic and spectroscopic characterization can produce comparable results, thus validating microscopic carrier lifetime analysis for thin-film solar cells.

For bilayer absorber with CdSeTe and CdTe semiconductors (Figure 1), we compare and contrast recombination in these two regions. This is enabled by correlative near-interface (above bandgap excitation) and bulk (two photon excitation, 2PE) time-resolved carrier lifetime microscopy. Our results provide direct experimental evidence that recombination lifetimes and doping (due to compensation described by the net acceptor density, N_A) are more uniform in CdSeTe and GB recombination losses in CdSeTe are reduced. This finding identifies the mechanism of PV performance improvement in CdSe/CdTe bilayer solar cells.^[16,21,22]

2. Results

2.1. PL Emission Spectra and External Radiative Efficiency

Figure 2 shows PL emission spectra when excitation fluence is equal to 1 Sun (2×10^{17} photons $\text{cm}^{-2}\text{s}^{-1}$) for solar cells with and without Al_2O_3 passivation. Excitation fluence-dependent spectrally integrated data shown in the inset can be fit to a power law $\text{PL} \propto (\text{excitation})^a$, where exponent $a = 1.7 \pm 0.1$ implies that the dominant recombination pathway is nonradiative SRH recombination.^[23] Based on emission peak energy of 1.40 eV, PL emission is attributed to near-interface CdSeTe region (Figure 1). An increase in PL intensity by $2.2\times$ (approximately constant at 0.2–14 Suns) when Al_2O_3 is applied at the back contact confirms back contact recombination losses. Therefore, recombination losses not only in CdSeTe, but also in CdTe and at the back contacts need to be considered. We analyze such losses using time-resolved measurements.

The external radiative efficiency (ERE) is obtained using spectral integration^[24] and is found to be $(0.05 \pm 0.01)\%$ for Al_2O_3 passivated sample and $(0.03 \pm 0.01)\%$ for sample without

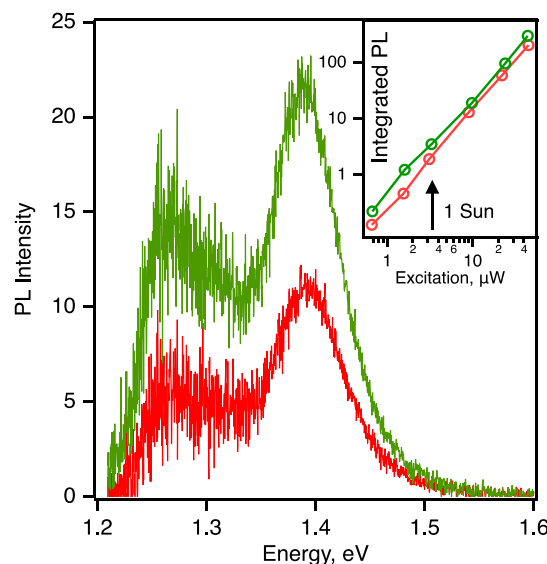


Figure 2. PL emission spectra for CdSe/CdTe samples with sputtered Al_2O_3 (green) and without passivation (red) measured at photon flux equal to 1 Sun (2×10^{17} photons $\text{cm}^{-2}\text{s}^{-1}$) using 632.8 nm excitation. Inset shows integrated PL intensity versus excitation fluence.

passivation. As described in the next section, with Al_2O_3 carrier lifetimes increase proportionally to ERE.

2.2. TRPL Spectroscopy

Figure 3a,b shows injection-dependent TRPL decays when excitation wavelength was 640 nm. For thin-film (3 μm -thick absorbers) solar cells PL time scale of 2 μs and lifetimes >300 ns are remarkable, exceeding earlier results for CdTe solar cells by an order of magnitude.^[11,12,25]

Charge carrier dynamics in CdTe solar cells is complex, but two-exponential fitting model where dynamics is described by lifetimes $\tau_{1,\text{TRPL}}$ and $\tau_{2,\text{TRPL}}$ is commonly used.^[26–29] The same model is applied to other thin-film solar cells.^[30,31] The primary goal is to separate early-time dynamics (“ $\tau_{1,\text{TRPL}}$ ”) when charge carrier spatial distribution is time-dependent due to drift and diffusion in the space charge field of the pn junction and longer-time dynamics (“ $\tau_{2,\text{TRPL}}$ ”) when carrier spatial distribution is

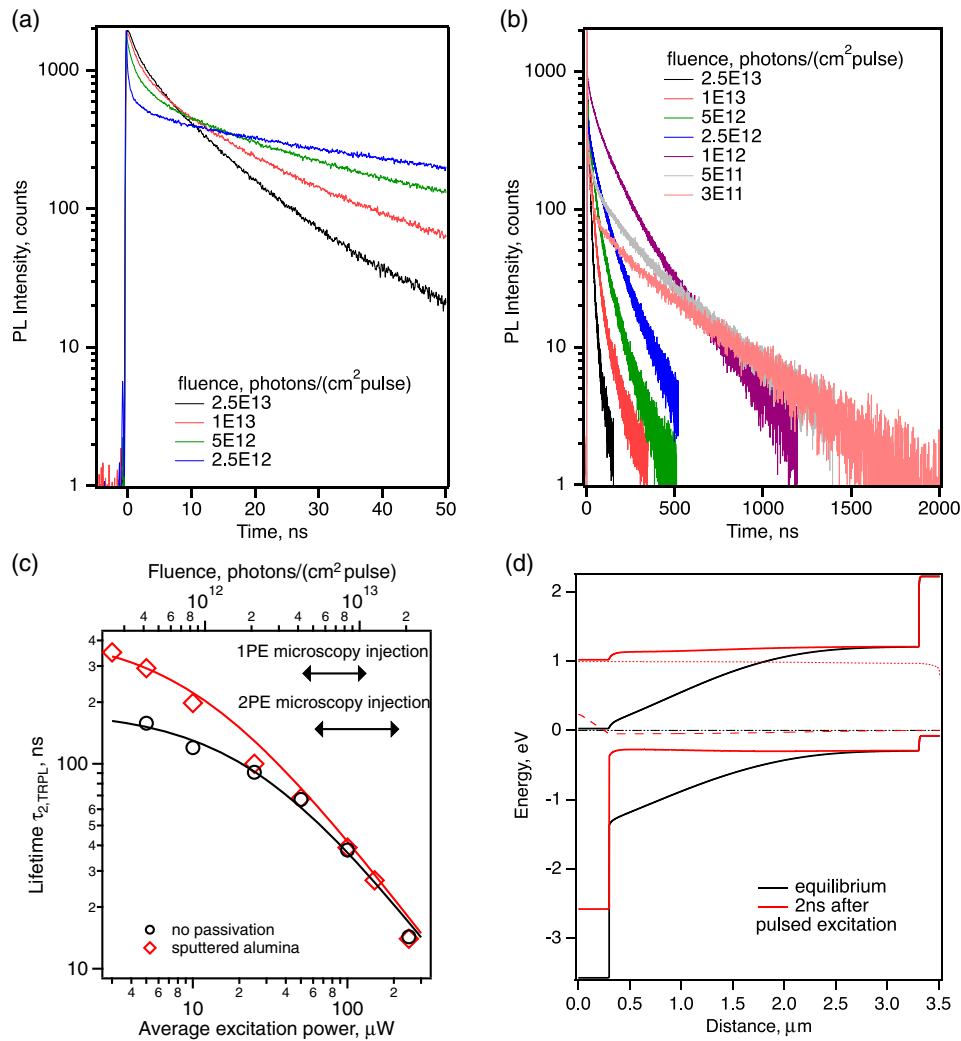


Figure 3. a,b) Injection-dependent TRPL decays for CdTe solar cells with Al_2O_3 . Data are shown on different time scales: a) “ $\tau_{1,\text{TRPL}}$ ” time scale and b) “ $\tau_{2,\text{TRPL}}$ ” time scale. c) Lifetimes $\tau_{2,\text{TRPL}}$ determined as described in the text for solar cells without passivation (black) and with Al_2O_3 passivation (red). Solid lines show fits to Equation (1). Data points and fits show injection ranges in spectroscopic measurements (data are averaged over $\approx 3000 \mu\text{m}^2$ area). In addition, arrows show injection ranges in 1PE and 2PE TRPL microscopy (averaged over $\approx 1 \mu\text{m}^2$ area) described in Section 2.3 and 2.4. d) Comparison of band diagrams in equilibrium (black, also shown in Figure 1b) and 2 ns after pulsed excitation (red).

approximately constant. When measured with high time resolution, processes described by $\tau_{1,\text{TRPL}}$ and $\tau_{2,\text{TRPL}}$ sometimes require more complex fitting, but distinction of time-dependent and constant carrier spatial distributions on $\tau_{1,\text{TRPL}}$ and $\tau_{2,\text{TRPL}}$ time scales still applies.^[26–29]

Analysis on the $\tau_{1,\text{TRPL}}$ time scale requires semiconductor device modeling because electron and hole drift has complex dependence on doping, band offsets, and other material and device parameters.^[26,27,32,36] As we describe below, analysis of $\tau_{2,\text{TRPL}}$ dynamics can be simplified.

We first apply $\tau_{1,\text{TRPL}}/\tau_{2,\text{TRPL}}$ model to the low-injection data. The first component of the decay $\tau_{1,\text{TRPL}} < 1$ ns (in reported studies and in samples studied here) is attributed to drift in the space charge field of the junction, interface recombination, and bulk recombination.^[26–28] In high-efficiency solar cells drift rate is higher than recombination rate, which is evident from $\tau_{1,\text{TRPL}}$ increase to 2.2 ns at higher injection (Figure 3a) due to screening

of the pn junction field by photogenerated carriers and resulting lower drift rate. From $\tau_{1,\text{TRPL}} \approx 0.5$ ns, we estimate charge carrier mobility $\mu = l \tau_{1,\text{TRPL}}^{-1} E_{\text{SCF}}^{-1}$, where space charge field strength $E_{\text{SCF}} \approx 6000 \text{ Vcm}^{-1}$ and depletion width $l \approx 1.5 \mu\text{m}$ are from the equilibrium band diagram in Figure 1b. The estimated $\mu \approx 50 \text{ cm}^2 \text{ V}^{-1} \text{ s}^{-1}$ is similar to mobility measured with light-induced transient grating for polycrystalline CdSeTe heterostructures^[24] and for compensated CdTe single crystals.^[33] We also estimated similar mobility for earlier-generation CdTe solar cells with CdS buffer.^[29] Therefore, ternary CdSeTe alloy has similar intragrain mobility as polycrystalline CdTe. (Transport across GBs is not considered on < 1 ns time scale for $> 1 \mu\text{m}$ crystalline grains.) High-efficiency thin-film solar cells have columnar grains, therefore intragrain mobility is relevant for solar cell analysis. Approximately 5–10 times higher mobility was measured for CdTe epitaxial heterostructures,^[18,20] therefore in principle it is possible to increase carrier diffusion length by increasing

mobility. However, recombination lifetimes span broader range and have larger effect on the diffusion length.

Next, we consider $\tau_{2,TRPL}$ dynamics. This analysis can be simplified due to carrier redistribution after the pulsed excitation. As shown in the band diagram in Figure 3d and 2 ns after the laser pulse space charge field strength is reduced, and conduction/valence bands are close to flat band conditions. This feature allows using analytical recombination rate model

$$\frac{1}{\tau_{2,TRPL}} = \frac{1}{\tau_B} + \frac{1}{\tau_{front}} + \frac{1}{\tau_{back}} + \frac{1}{\tau_{rad}} \quad (1)$$

where τ_B is bulk SRH recombination lifetime, τ_{front} and τ_{back} are effective lifetimes to describe front and back interface recombination. Radiative lifetime is $\tau_{rad} = (B \times (N_A + \text{injection}))^{-1}$, where radiative recombination coefficient is taken to be $B = 1 \times 10^{-10} \text{ cm}^3 \text{ s}^{-1}$.^[34]

Transition from low- to high-injection regimes is described by characteristic $\tau_{2,TRPL}$ intensity dependence in Figure 3c. Some aspects of this data can be approximated by Equation (1). Extrapolating to low injection (when excitation fluence $< 5 \times 10^{11} \text{ photons cm}^{-2} \text{ pulse}^{-1}$) allows determination of the SRH recombination lifetime τ_{SRH} , which includes interface and bulk recombination.

Fits shown in Figure 3c predict $\frac{1}{\tau_{SRH,Al_2O_3}} = \frac{1}{\tau_B} + \frac{1}{\tau_{front}} + \frac{1}{\tau_{back,Al_2O_3}} = 1/(428 \pm 19 \text{ ns})$ for passivated sample and $\frac{1}{\tau_{SRH}} = \frac{1}{\tau_B} + \frac{1}{\tau_{front}} + \frac{1}{\tau_{back}} = 1/(181 \pm 11 \text{ ns})$ for sample without passivation. If we attribute τ_{SRH} increase from 181 to 428 ns to reduced back contact recombination due to passivation with Al_2O_3 , then

$$\frac{1}{\tau_{2,low}} - \frac{1}{\tau_{2,low,Al_2O_3}} \approx \frac{S_{back} - S_{back,Al_2O_3}}{d} \quad (2)$$

where $d = 3 \mu\text{m}$ is thickness of the absorber and S_{back} is recombination velocity. Using $S_{back,Al_2O_3} \approx 200 \text{ cm s}^{-1}$ (determined for Al_2O_3 passivated polycrystalline heterostructures),^[35] Equation (2) yields estimate for effective $S_{back} = (1.0\text{--}1.5) \times 10^3 \text{ cm s}^{-1}$. Mechanism of such passivation requires further analysis. In addition to defect passivation, electronic barriers in the device might limit electron drift to the back contact and in this way reduce recombination.^[36]

Figure 3c also shows injection ranges in TRPL microscopy (see next sections). We estimate injection in microscopic measurements by spatially averaging all data in the microscopy scan, fitting kinetic data to the two-exponential decay model, and comparing lifetime $\tau_{2,TRPL}$ with the corresponding data measured with a larger laser beam. With shorter integration time and smaller excitation volume (volume from which radiative emission is collected), it is not possible to reach lowest injection range in microscopic measurements. Therefore, spectroscopic and microscopic carrier lifetime characterization is complementary—spectroscopy allows broader injection range necessary to determine SRH lifetime, whereas microscopy allows characterization of the spatial recombination lifetime distributions. Higher injection is possible in 2PE microscopy (when compared with 1PE microscopy) due to greater sample stability when focused fs laser pulses are applied with photon energies less than the bandgap.

2.3. 2PE TRPL Microscopy

Figure 4 shows 2PE TRPL microscopy data ($25 \times 25 \mu\text{m}^2$ field of view, TRPL decays measured every $0.5 \mu\text{m}$). Because absorption coefficient at 2PE excitation wavelength (1030 nm) is low, with 2PE carriers are generated uniformly in the bulk of the absorber. The data are represented as a time-dependent image stack with $\Delta t = 0.1 \text{ ns}$. The time-integrated (a) and first (b, $t = 0$, immediately after the laser excitation) frames are illustrated. As in spectroscopy, injection dependence was studied. Because PL intensity dependence on injection is described by the power law, intensity differs by orders of magnitude and images in Figure 4 are normalized. The scale bars show that intensity range is reduced at higher injection (see Section 3 for quantitative analysis). Multidimensional TRPL microscopy data (x , y , and time dimensions) can be analyzed as single pixel decays (shown in (c) and (d)), as linear time-dependent intensity profiles (shown in (e) and (f)), and as lifetime histograms for all pixels (shown in (g) and (h)). Such representations show complimentary aspects of recombination dynamics in CdTe absorber bulk.

Figure 4c,d shows the comparison of low- and high-injection single pixel and averaged kinetics. The figure shows several pixels where amplitudes and lifetimes differ the most at respective excitation conditions. Pixel and averaged decays are similar at high injection. In contrast, low-injection PL amplitudes at $t = 0$ differ up to 10 times.

Figure 4e,f shows representative time-dependent line scan data. At low injection, high contrast is present at $t = 0$, and contrast decreases over time. As shown in Section 3, such data indicate nonuniform hole (majority carrier) density N_A in CdTe. Data in Figure 4e also show that pixels where N_A is higher have shorter lifetimes. The typical width of features with differing PL intensity is $2\text{--}5 \mu\text{m}$, consistent with crystalline grain sizes in solar cells studied here. At high-injection (Figure 4f), PL spatial dependence and recombination rates are much more uniform at $t = 0$ and over time.

To illustrate recombination lifetime variation throughout $25 \times 25 \mu\text{m}^2$ area, we fit the data to the two-exponential decay model ($A_1 \exp(-t/\tau_{1,a}) + A_2 \exp(-t/\tau_{1,b})$, where A_1/A_2 are amplitudes and $\tau_{1,a}/\tau_{1,b}$ are lifetimes) and plot lifetime $\tau_{1,a}/\tau_{1,b}$ distributions in Figure 4g,h. Because carriers are mobile, fitting is limited to $< 15 \text{ ns}$ when bulk-generated carriers are less affected by the back-interface recombination. Because fits in Figure 4g,h are not applied to full decays but only $0\text{--}15 \text{ ns}$ range, exponential components $\tau_{1,a}/\tau_{1,b}$ describe spatially dependent carrier dynamics described in Section 2.2 ($\tau_{1,TRPL}$). To further reduce impact of back-contact recombination, Al_2O_3 passivation was used. Such lifetime distributions are shown at different injections, which correspond to images in Figure 4a,b.

Several trends are evident in 2PE TRPL lifetime $\tau_{1,a}$ and $\tau_{1,b}$ histograms. First, low-injection lifetimes span broad range, < 0.1 to 1.2 ns for $\tau_{1,a}$ and 2 to 10 ns for $\tau_{1,b}$. Initially, $\tau_{1,a}$ and $\tau_{1,b}$ increase with injection (up to $1.7 \times 10^{18} \text{ photons cm}^{-2} \text{ pulse}^{-1}$ fluence), which indicates increasing defect screening. When fluence is 2.6×10^{18} and $4.4 \times 10^{18} \text{ photons cm}^{-2} \text{ pulse}^{-1}$, lifetimes become shorter, which indicates transition to radiative recombination regime. Consistent with transition from defect screening to radiative recombination, lifetime distributions

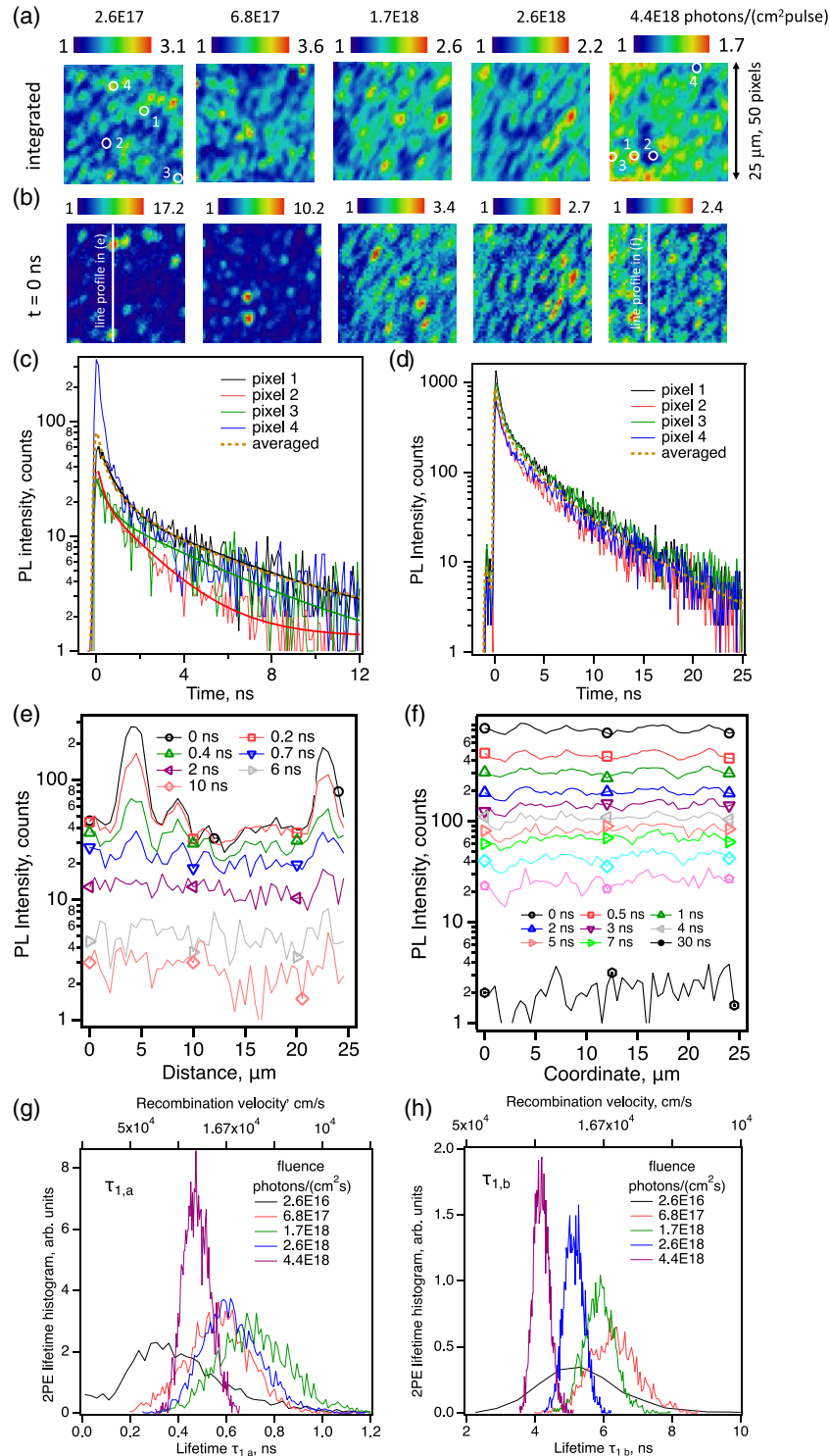


Figure 4. 2PE TRPL microscopy data for Cu-doped CdSe/CdTe solar cells. a) Time-integrated normalized PL images and b) the first frame at $t = 0$ ns. Scale bars show intensity range in each image. Excitation fluence is indicated in photons/(cm^2 pulse). c,d) Single-pixel kinetic decays measured at the c) lowest and d) highest injection. Pixel locations are illustrated in (a). Dashed lines in (c,d) show spatially averaged TRPL decays. e,f) Representative time-dependent line scans measured at the (e) lowest and (f) highest injection. Linear profile locations are indicated in (b). Time delays after excitation are given in legends. g,h) Lifetime and recombination velocity distributions for injection-dependent 2PE TRPL data in (a,b). Data are fit on 0–15 ns time scale using two-exponential decay model. The distributions of the first decay component $\tau_{1,a}$ are shown (g) and distributions for the second decay component $\tau_{1,b}$ in (h). Excitation fluence (photons cm^{-2} pulse $^{-1}$) is shown in the legends.

become narrower (at high injection, photogenerated electrons and holes recombine with similar rates at all pixels). Therefore, for defect analysis, low-injection data are the most important. The same result was obtained from spectroscopic measurements (Figure 3).

Lifetimes in Figure 4g,h can be described by effective recombination velocities $S_{\text{effective}} = d/\tau \approx (1-5) \times 10^4 \text{ cm s}^{-1}$, estimated using distance parameter $d = 0.1 \mu\text{m}$ in (g) and $d = 1 \mu\text{m}$ in (h). Such recombination velocities are typically found from cathodoluminescence (CL) data modeling for CdTe absorbers.^[37–39] In Section 3, we use GB defect screening model to quantitatively evaluate 2PE TRPL microscopy results.

2.4. 1PE TRPL Microscopy

Time-resolved microscopy with excitation at 515 nm was used to generate carriers near the front interface, in the CdSeTe region of the absorber (absorption depth $1/\alpha_{515 \text{ nm}} = 0.13 \mu\text{m}$, $\alpha_{515 \text{ nm}}$ is absorption coefficient). Time-integrated and $t = 0$ images in Figure 5a,b show that PL intensity and initial amplitude are very uniform over the $25 \times 25 \mu\text{m}^2$ area. The intensity contrast is only 1.8–1.9 at the lowest injection and further decreases to 1.5–1.6 at higher injection. Therefore, data indicate different carrier dynamics in CdSeTe (Figure 5) than in CdTe (Figure 4). To describe injection-dependent 1PE TRPL dynamics, we analyze single pixel TRPL decays (Figure 5c,d) and time-dependent intensity histograms (Figure 5e).

Figure 5c,d shows the comparison of spatially averaged and single pixel TRPL data. The two pixels illustrated in (c) and (d) represent shortest and longest lifetimes in a respective image, where pixel lifetimes differ by $\leq 10\%$. Such comparisons show that 1PE TRPL data depends more strongly on injection than it varies spatially at a given injection.

Due to small recombination lifetime variation, we do not apply two-exponential fitting model to 1PE TRPL microscopy results (four adjustable parameters can be overfit) but analyze time-dependent PL intensity histograms in Figure 5e. To measure full width at half maximum (FWHM), data were fit with Gaussian functions and Gaussian FWHM versus photon fluence are shown in the inset. Time-integrated and $t = 0$ histograms have the same FWHM. This means PL contrast is already present at $t = 0$ and contrast remains constant in time. Because contrast is time-independent, it is attributed to N_A variation, not lifetime variation (see Section 3). Because contrast is low, N_A heterogeneity is low in the near-interface CdSeTe absorber. This heterogeneity can be described as $\text{FWHM} \leq 0.25$ (of average PL intensity), or intensity variation less than two times.

As shown in the inset of Figure 5e, PL intensity histogram FWHM decreases at higher injection. Such data indicates transition from low to high injection, and the same trend was observed in 2PE TRPL lifetime data in Figure 4g,h. Transition from SRH to radiative recombination regimes is observed at similar injections in 1PE and 2PE TRPL microscopy data, which indicates similar N_A in near-interface CdSeTe and in CdTe bulk. The difference is that N_A is spatially heterogeneous in CdTe bulk but much more uniform in CdSeTe.

Finally, Figure 5f shows time- and spatially integrated PL intensity versus 515 nm excitation fluence. These data are described by a power law, where exponent $a = 1.8 \pm 0.1$ is very similar to results where constant wave (not pulsed) excitation equivalent to 0.2–14 Suns was used (Figure 2, $a = 1.7 \pm 0.1$). Because the power law exponent indicates recombination mechanism,^[23] comparison shows that time-resolved microscopy data are measured at conditions similar to solar excitation.

3. Discussion

3.1. Voltage Losses Due to Nonradiative SRH Recombination

From injection-dependent TRPL measurements (Figure 3), we determined SRH recombination lifetimes $\tau_{\text{SRH}} = 181 \pm 11 \text{ ns}$ in samples without back-contact passivation. Reported lifetimes for Cu-doped solar cells range from 2 ns in for CdTe absorbers^[11,29] to 10–30 ns for alloyed CdSe/CdTe absorbers.^[12,25,40] However, even with increased lifetimes, recombination is dominated by defects. Experiments and theoretical analysis suggest that recombination center defects can be related to Cu incorporated differently than Cu_{Cd} (p-type dopant Cu_{Cd} activation is $< 1\%$,^[41] and Cu impurities can introduce recombination centers).^[42,43] Nonradiative SRH recombination leads to voltage losses, and voltage in CdTe solar cells is only 77% of the SQ limit. To quantify voltage losses, we determine qFLS by relating lifetimes to minority carrier (electron) density^[44,45] and use hole density from capacitance voltage (CV)

$$e \text{ qFLS} = E_g + k_B T \ln \left(\frac{n_e N_A}{N_C N_V} \right) \quad (3)$$

where e is elementary charge, k_B is Boltzmann's constant, T is temperature, n_e is excess electron density at 1 Sun, $N_C = 8 \times 10^{17} \text{ cm}^{-3}$ is density of states in the conduction band, and $N_V = 1.8 \times 10^{19} \text{ cm}^{-3}$ is density of states in the valence band.^[46] Assuming uniform carrier density in $d = 3 \mu\text{m}$ thick absorber, $2 \times 10^{17} \text{ cm}^{-3}$ photons $\text{cm}^{-2} \text{s}^{-1}$ irradiation (equivalent to 1 Sun for 1.42 eV bandgap), and $\tau_{\text{SRH}} = 181 \text{ ns}$, estimated $n_e \approx 1.2 \times 10^{14} \text{ cm}^{-3}$. The same value $n_e = G\tau_{\text{SRH}} \approx 1.2 \times 10^{14} \text{ cm}^{-3}$ is obtained if we approximate generation rate G from the short-circuit current $J_{\text{SC}} = 31 \text{ mA cm}^{-2}$ as $G = J_{\text{SC}}/(ed)$.^[45] Using $N_A = (1-3) \times 10^{14} \text{ cm}^{-3}$ from CV,^[40] Equation (3) predicts qFLS = 880–905 mV. Estimate is in good agreement with $V_{\text{OC}} = 887 \text{ mV}$ for the record-efficiency solar cell^[6] and $V_{\text{OC}} = 903 \text{ mV}$ for the record-voltage solar cell.^[40] This agreement suggests that for Cu-doped CdSe/CdTe solar cells other losses (e.g., due to band tails and due to contact selectivity) are much lower and nonradiative SRH recombination due to semiconductor defects is by far the largest contributor to V_{OC} losses.

Defect-mediated SRH recombination occurs at interfaces and in the semiconductor bulk, and bulk/interface recombination rates are additive as described by Equation (1). We can evaluate back-contact recombination losses from measurements on passivated samples. Passivation with Al_2O_3 increases recombination lifetime to $\tau_{\text{SRH}} = 428 \pm 19 \text{ ns}$,

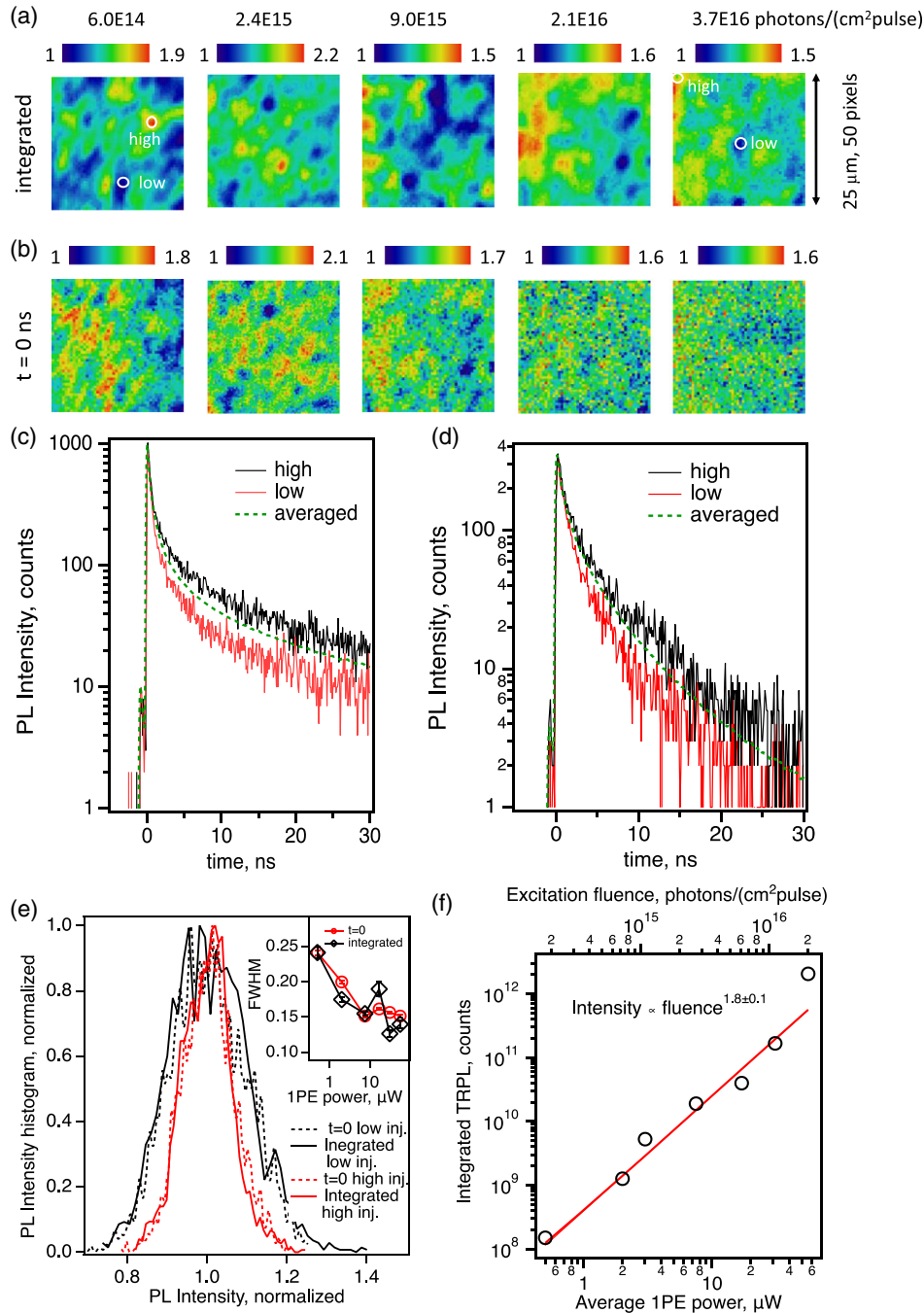


Figure 5. 1PE TRPL microscopy data for Cu-doped CdSe/CdTe solar cells. a) Normalized PL images integrated over time and b) at $t = 0$. Scale bars show intensity range in each image. Excitation fluence is indicated in photons $\text{cm}^{-2} \text{pulse}^{-1}$. c,d) Single-pixel kinetic decays measured at the c) lowest and d) highest injection. High and low pixel locations are indicated in (a). Dashed lines show spatially averaged TRPL decays. e) Time-integrated and $t = 0$ PL intensity histograms for the lowest (black) and highest (red) injection. Inset shows FWHM for $t = 0$ (red circles) and for time-integrated (black diamonds) PL intensity histograms versus injection. f) PL intensity versus average excitation power and excitation photon fluence.

and proportionally increases n_e . According to Equation (3), for passivated samples $q\text{FLS}_{\text{Al}_2\text{O}_3} = 906\text{--}931 \text{ mV}$, or 26 mV higher.

Radiative efficiency also describes recombination losses in solar cells.^[9] Unlike carrier lifetimes,^[11,12,14–18,20,22,24,29,33–35,40,43] radiative efficiencies are rarely reported for CdTe,^[24] likely due

to high surface recombination velocity which significantly impacts ERE measurements. Here, we report $\text{ERE} = (3\text{--}5) \times 10^{-4}$ from calibrated PL spectral measurements (Figure 2).

It is also possible to estimate radiative efficiency from lifetime data. We start with the internal radiative efficiency (IRE).

Radiative lifetime $\tau_R = 1/(BN_A) = 33\text{--}100\ \mu\text{s}$ for $N_A = (1\text{--}3) \times 10^{14}\ \text{cm}^{-3}$, and IRE can range from the low value of $\text{IRE} = \tau_{\text{SRH}}/(\tau_{\text{SRH}} + \tau_R) = 1.8 \times 10^{-3}$ ($\tau_{\text{SRH}} = 188\ \text{ns}$, $\tau_R = 100\ \mu\text{s}$) to the high value 1.3×10^{-2} ($\tau_{\text{SRH}} = 428\ \text{ns}$, $\tau_R = 33\ \mu\text{s}$). ERE combines IRE and outcoupling, $\text{ERE} = \text{IRE} \times \text{OUT}$. For polycrystalline absorbers, estimates for outcoupling will be approximate. Yablonovitch et al. have shown^[47] that for substrate/absorber structure (in this study substrate is glass, Figure 1), $\text{OUT} \approx (n_{\text{glass}}^2 + 1)/2n_{\text{CdTe}}^2 = 0.18$, where n_{glass} and n_{CdTe} are refractive indexes for glass and absorber. Therefore, as calculated from lifetime and doping data, ERE can range from 3×10^{-4} to 2×10^{-3} . Experimental ERE values agree with the lower range of this estimate, perhaps due to uncertainty in determining outcoupling from nonsmooth polycrystalline semiconductor layers.

Therefore, both carrier lifetime and radiative efficiency indicate $\Delta V_{\text{OC}} \approx -250\ \text{mV}$ SRH recombination losses in Cu-doped CdSe/CdTe solar cells. About 26 mV of these losses can be recovered with the passivating back contact. Such improvement would be significant and can help overcome long-standing $V_{\text{OC}} = 900\ \text{mV}$ limitation.^[40] However, dominant SRH recombination losses must be attributed to the front interface and especially the bulk of the absorber. Further voltage improvements require increasing bulk recombination lifetimes and doping, which are the areas of active research.^[25,78]

Next, we analyze efficiency and V_{OC} -limiting bulk recombination from the time-resolved microscopy data.

3.2. Mapping Recombination Lifetimes and Net Acceptor Density from TRPL Microscopy

Previous section identified dominant SRH recombination and quantified resulting voltage losses. For that analysis, spectroscopic PL and TRPL measurements were spatially averaged over many crystalline grains. In polycrystalline solar cells we also need to consider spatial recombination lifetime and net acceptor density variation (both n_e and N_A determine V_{OC} , Equation (3)). Here, we show that TRPL microscopy allows such characterization from PL amplitudes at $t = 0$ (time of excitation before recombination) and TRPL lifetimes.

Radiative recombination rate described by $\text{PL}(t, x, y)$ at time t and coordinates (x, y) depends on electron density $n(t, x, y)$ and hole density $p(t, x, y)$

$$\text{PL}(t, x, y) = Bn(t, x, y)p(t, x, y) \quad (4)$$

Immediately after the excitation ($t = 0$) in the case of low injection, this expression simplifies to

$$\text{PL}(t = 0, x, y) = Bn(t = 0)N_A(x, y) \quad (5)$$

where $n(t = 0)$ is the photoinjected minority carrier density, which is the same for all pixels, and $N_A(x, y)$ is the net acceptor (dopant) density. Therefore, according to Equation (5), low-injection PL at $t = 0$ describes spatial $N_A(x, y)$ distribution multiplied by a constant $Bn(t = 0)$. “Dopant mapping” with Equation (5) is only possible at $t = 0$. At $t > 0$, recombination reduces minority carrier density and it is not possible to separate recombination and doping variation in the $n(t, x, y)N_A(x, y)$

product. Ability to use Equation (5) to map $N_A(x, y)$ distribution illustrates advantage of TRPL imaging.

In contrast, when injection is high, electron and hole densities are equal and according to Equation (4) PL intensity at $t = 0$ is:

$$\text{PL}(t = 0, x, y) = Bn^2(t = 0) \quad (6)$$

According to Equation (6), high-injection PL images at $t = 0$ will have constant intensity. Data in Figure 4 and 5 agrees with Equation (5) and (6)—low-injection PL at $t = 0$ indicates nonuniform hole distribution, and at high-injection PL at $t = 0$ are more uniform at all (x, y) coordinates. More uniform microscopic PL intensity as described by Equation (6) also allows identification of the high-injection conditions.

Next, we apply model of Equation (5) and (6) to time-resolved microscopy data with excitation of near-interface CdSeTe (Figure 5, 1PE) and CdTe bulk (Figure 4, 2PE).

3.3. Contrasting CdSeTe and CdTe Electro-Optical Properties

In this section, we discuss $\text{PL}(t = 0, x, y)$ amplitude data, which maps net acceptor density $N_A(x, y)$ in CdSeTe and CdTe absorbers. PL images at $t = 0$ indicate substantial $N_A(x, y)$ variation in CdTe. According to Figure 4b and Equation (5), the N_A in CdTe varies $\approx 17\times$ over the $25 \times 25\ \mu\text{m}^2$ area. Such N_A variation can be due to nonuniform Cu_{Cd} (p-type dopant) distribution or due to hole (majority carrier) depletion. Because $\text{PL}(t = 0, x, y)$ heterogeneity decreases at higher injection, data are consistent with hole density variation due to depletion. It is widely accepted that depletion in CdTe is caused by charged GBs.^[48,49] We assume this attribution in further analysis. If depleted regions were related not only to charged GBs but also to other charged extended defects, the impact on recombination and solar cell performance would be similar.

Figure 6a shows depleted GBs and their impact on carrier dynamics. Carrier diffusion length (we use mobility μ from spectroscopic measurements, see Section 2) $L_d = \sqrt{\frac{k_B T}{e} \mu \tau} = 5\text{--}7\ \mu\text{m}$ exceeds crystalline grain size and after drift in the GB space charge field carriers are trapped or recombine near GBs. Trapping can lead to GB defect saturation. Traps attributed to GBs have been identified from time-resolved CL at low temperature.^[50] Nonmicroscopic room temperature PL also indicated interface trap states.^[34] Charged donor and acceptor defects at GBs were assumed in CdTe solar cell modeling, and it was shown that different GB defect distributions lead to similar V_{OC} losses.^[51–53]

When photogenerated carrier density exceeds trap density, GB potentials are screened. Reduced GB potentials at higher injection are indicated as dashed lines in Figure 6a. We analyze this data quantitatively from lifetime distributions (next section).

The charged GB screening model applies to bulk CdTe and near-interface CdSeTe, but $N_A(x, y)$ (and also lifetime) distributions are much more uniform in CdSeTe. While $\text{PL}(t = 0, x, y)$ data and therefore $N_A(x, y)$ varies by $17\times$ in CdTe (2PE data, Figure 4), this range is $< 2\times$ in CdSeTe (1PE data, Figure 5).

Our results help understand high CdSeTe radiative efficiency in solar cells^[16,21,25,54] and in polycrystalline heterostructures.^[24,35,55] Radiative efficiency can increase due to reduced

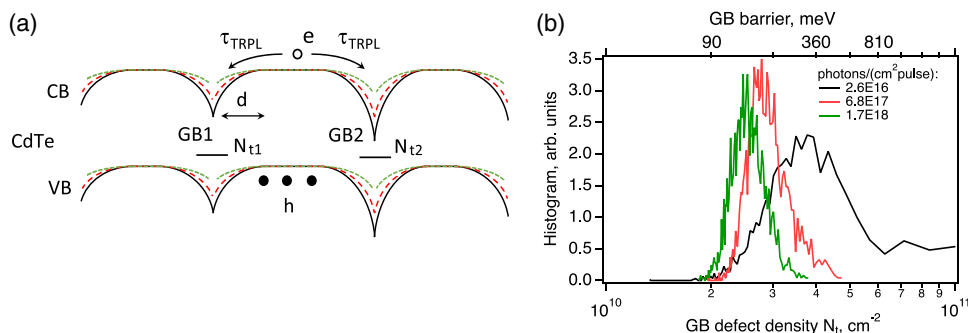


Figure 6. a) Illustration of charge carrier dynamics near charged GBs. At the lowest injection, GB barriers are described by solid lines and lifetimes are short due to drift in the strong space charge field. As field strength is reduced due to photoinjection lifetimes increase proportionally. This mechanism dominates microscopic TRPL data in CdTe but is much weaker in the CdSeTe absorber region. b) Distribution of GB defect density (bottom axis) and GB barrier heights (top axis) calculated from TRPL lifetimes in Figure 4g as described in the text.

point defect density, and also due to reduced trapping and recombination at GBs and other extended defects. First, we briefly summarize point defect models. It is assumed that CdSeTe point defects^[56] are similar to those for CdTe,^[42,46,57,58] with the bandgap modification from 1.5 eV (CdTe) to 1.4 eV (CdSeTe).^[59] Bandgap adjustment changes defect energies, and some midgap defect states can become shallower, thus reducing SRH recombination rates due to such more shallow defects. But it is not clear if changing defect energy by 0.1 eV is sufficient for the radiative efficiency increase by a factor of at least five.^[16,21,25,60] Contrasting bulk recombination properties are especially clear in Al₂O₃ passivated heterostructures (without a bilayer absorber and without the pn junction space charge field) where lifetimes are more than ten times higher for CdSeTe (430 ns) than for CdTe (27 ns).^[55]

In summary, we suggest that in addition to SRH recombination center point defects such as Te_{Cd},^[57,58] Cu_{Cd},^[42] and others,^[46,56,61,62] CdSe/CdTe defect models also need to consider the origin and impact of charges at extended defects, including GBs.

The model of increased recombination due to charged extended defects is also consistent with results for epitaxial Cd(Se)Te, where improvement in lifetimes and radiative efficiencies was attributed to reduced extended defect densities.^[63] Using optical electric field induced second harmonics (EFISH) imaging, we showed that stacking fault extended defects have space charge fields,^[20] but there are no space charge fields for threading dislocations.^[64] As a result, recombination is increased for heterostructures with (charged) stacking faults and reduced for comparable densities of (electrically neutral) threading dislocations.^[20,63,64]

Therefore, in both polycrystalline and epitaxial Cd(Se)Te charged extended defects are important for recombination and V_{OC} losses. We now examine recombination rates near such defects.

3.4. Space Charge Field Screening and Microscopic Carrier Lifetimes

Here, we analyze microscopic carrier lifetimes. As described earlier, lifetimes are more uniform in near-interface CdSeTe (1PE

data, Figure 5), which we attribute to reduced charged extended defect densities. In contrast, we observe large recombination lifetime variation for CdTe, which constitutes bulk of the absorber. Such variation is largest at the lowest injection, when $\tau_{1,a} = 0.1$ –1.2 ns and $\tau_{1,b} = 2$ –10 ns (lifetime histograms in Figure 4g,h). When injection is increased and space charge fields are gradually screened, lifetimes become more uniform. For example, at 1.7×10^{18} photons cm $^{-2}$ pulse $^{-1}$ fluence, $\tau_{1,a} = 0.4$ –1.2 ns and $\tau_{1,b} = 4$ –8 ns. To understand the relationship between the photon fluence (injection) and carrier lifetimes, we use literature model for electrostatic potentials at charged extended defects.^[65,66] According to this model, the potential barrier height Φ_B is given by^[65,66]

$$\Phi_B = \frac{eN_t^2}{8\epsilon\epsilon_0N_A} \quad (7)$$

where ϵ is static dielectric constant, ϵ_0 is vacuum permittivity, and N_t is trap density per unit area (units cm $^{-2}$). If we assume that the fastest components of 2PE TRPL decay (Figure 4g) are due to the drift in the GB space charge field (field strength E), then $\tau_{1,a} \approx d/\mu E$, where d is depletion width is μ is mobility. Using the simplest approximation, the field strength $E \approx \Phi_B/d$. Therefore, lifetimes $\tau_{1,a}$ indicate charged defect density according to

$$N_t = \sqrt{\frac{8\epsilon\epsilon_0N_Ad^2}{e\mu\tau_{1,a}}} \quad (8)$$

The model of Equation (8) can be applied to lifetime $\tau_{1,a}$ histograms to determine extended defect density. Using Equation (7), such data can then be used to determine barrier heights. Results of both analyses are shown in Figure 6b. Data measured at the lowest fluence indicate defect density $N_t = (2$ – $10) \times 10^{10}$ cm $^{-2}$ and corresponding GB barrier range $\Phi_B = 90$ – 800 meV. GB potentials are screened to <360 meV at fluence of 6.8×10^{17} photons cm $^{-2}$ pulse $^{-1}$ and <200 meV at fluence of 1.7×10^{18} photons cm $^{-2}$ pulse $^{-1}$. Because microscopic lifetimes are measured with injection exceeding 1 Sun, GB barriers in solar cells are not screened and charged defects are important for solar cell analysis.^[51–53]

It is widely recognized that charged GBs impact CdTe solar cells.^[48,49,51–53] GB potential or barrier height measurements are difficult, in part because different experimental methods use different excitation/injection conditions and have different probing resolutions. For example, Kelvin probe scanning force microscopy (KPFM) was used to report GB potential histograms in CdTe solar cells, and after CdCl₂ treatment and Cu doping GB barrier heights ranged from 40 to 260 meV.^[67] This KPFM data is similar to $(0.68\text{--}1.7) \times 10^{18}$ photon cm⁻² pulse⁻¹ fluence results in Figure 6b, but we find 2–3 times higher barriers in measurements at the lowest injection. As a scanning probe technique, KPFM is very sensitive to surface properties. More recently, KPFM data for polycrystalline CdTe were interpreted to indicate surface potential spikes (40–80 meV range) deriving from electrostatic GB potentials deep in the absorber layer, but without Φ_B quantification.^[68] In contrast, EO microscopy reveals carrier dynamics attributed to electrostatic barriers in the buried absorber region, hundreds nm to micrometer from the transparent conductive oxide (TCO)/absorber interface.

Earlier we used EFISH microscopy to image electric field distribution in polycrystalline CdTe, but scale in that data was relative, not absolute.^[15,35] Scanning probe microwave reflectivity measurements of CdTe GB depletion were also not quantitative.^[69] Modeling showed that impact of charged GBs cannot be estimated from electron beam-induced current (EBIC) data.^[70] Overcoming such experimental challenges, injection-dependent microscopic lifetime model described here provides quantitative Φ_B estimates. When lifetimes are spatially averaged, they correctly estimate solar cell voltages.

Gaury and Haney presented analytical and numerical V_{OC} loss analysis due to charged GBs in CdTe solar cells.^[51–53] They analyzed columnar^[51] and “tilted” GBs^[53] with both single GB defects and GB defect distributions.^[52] In all cases, losses are small when GB recombination velocity $S_{GB} < 10^3$ cm s⁻¹. Losses increase to $\Delta V_{OC} \approx -50$ mV when $S_{GB} = 10^4$ cm s⁻¹ and reach $\Delta V_{OC} \approx -(100\text{--}150)$ mV when $S_{GB} = 10^5$ cm s⁻¹. When our data are described as recombination velocities, Figure 4g,h indicates $S_{GB} = (1\text{--}5) \times 10^4$ cm s⁻¹ range, depending on injection. Therefore, according to charged GB models,^[51–53] up to half of total V_{OC} losses in CdSe/CdTe solar cells can be attributed to charged GB recombination and carrier trapping in CdTe.

Our data enable comparisons to other thin-film solar cells. For example, charged GBs with $S_{GB} \leq 5 \times 10^3$ cm s⁻¹ (barrier heights $\Phi_B \leq 50$ mV) were identified as V_{OC} loss locations in 20.8% efficient Cu(In,Ga)Se₂ polycrystalline solar cells, and such losses were reduced with postdeposition treatments.^[71] In comparison, near-interface CdSeTe absorber can have similarly small S_{GB} (not resolvable in our measurements), but in CdTe absorber region S_{GB} is an order of magnitude larger. Therefore, control of GB chemistry with processes such as CdCl₂ treatment^[40] continues to be important for CdTe solar cells. Passivation of CdTe back contact also needs to consider GB properties.^[72]

4. Conclusion

We described electro-optical (EO) analysis methodology for thin-film solar cells and applied this analysis to the leading

thin-film PV technology, Cu-doped CdSe/CdTe solar cells. Carrier lifetimes ranged from ≈ 180 ns (without back contact passivation) to ≈ 430 ns (Al₂O₃ passivation) and indicated qFLS = 880–905 mV (no passivation) and 906–931 mV (Al₂O₃ passivation). These data show that it is possible to overcome long-standing 900 mV open-circuit voltage limitation^[40] by developing passivating contacts. Passivating contacts where initial efforts are already applied to CdTe solar cells include microstructured insulating Al₂O₃^[55] and tunneling contacts.^[73]

From lifetime and radiative efficiency analysis, we attributed the dominant voltage losses in Cu-doped CdSe/CdTe solar cells to nonradiative SRH recombination, with losses due to band tails and contact selectivity being much smaller.

Microscopic carrier lifetime measurements showed contrasting carrier dynamics in CdSeTe and CdTe, which was attributed to N_A and recombination lifetime heterogeneity in CdTe bulk and much lower heterogeneity in the near-interface CdSeTe. We showed that a model of charged and depleted GBs is consistent with carrier lifetime microscopy data. When using this model, data indicated CdTe GBs barrier heights from 100 to 900 meV, with the average value being in the 350 meV range. In contrast, defects creating space charge fields were largely passivated in ternary CdSeTe absorber. Therefore, in developing CdTe defect models, not only point defects but also charges at extended defects need to be considered.

Figure 7 summarizes EO properties and recombination loss locations in Cu-doped CdSe/CdTe solar cells. High carrier lifetimes and mobilities result in carrier diffusion length $L_d = 5\text{--}7$ μ m, which exceeds absorber thickness. Therefore, passivation is important not only for the front interface, but also for GBs and for the back contacts. Nondestructive EO measurements developed and applied in this study allow qualitative and quantitative analysis for such buried semiconductor layers and interfaces.

5. Experimental Section

Solar Cells: Solar cells were fabricated at First Solar by depositing thin films on the glass substrate.^[25,40] The solar cell device stack is TCO, CdSeTe, and CdTe bilayer absorber, ZnTe, and metal back contact (Figure 1). Postdeposition anneals introduced Cu and Cl into absorber. Typical solar cell performance reached $\approx 18\%$ power conversion efficiency and $V_{OC} \approx 845$ mV. Typical current density versus applied voltage and external quantum efficiency (EQE) data are shown in Figure 8.

Solar cells used graded absorber, where the near-interface bandgap of ≈ 1.4 eV was due to Se alloying in CdSeTe, and in the bulk CdTe bandgap was 1.50 eV.^[25] The bandgap spatial distributions in high-efficiency CdSeTe solar cells fabricated in different laboratories using semiconductor vapor transport deposition,^[25,40,74] close space sublimation,^[16,21] and evaporation^[75] were characterized with CL on bevel and cross-sectional

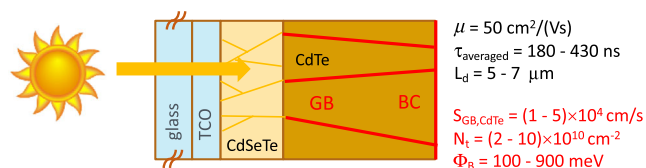


Figure 7. Illustration of recombination loss locations in bilayer CdSe/CdTe solar cells. Red lines indicate interfaces where recombination reduces carrier lifetime. GB is grain boundary; BC is back contact.

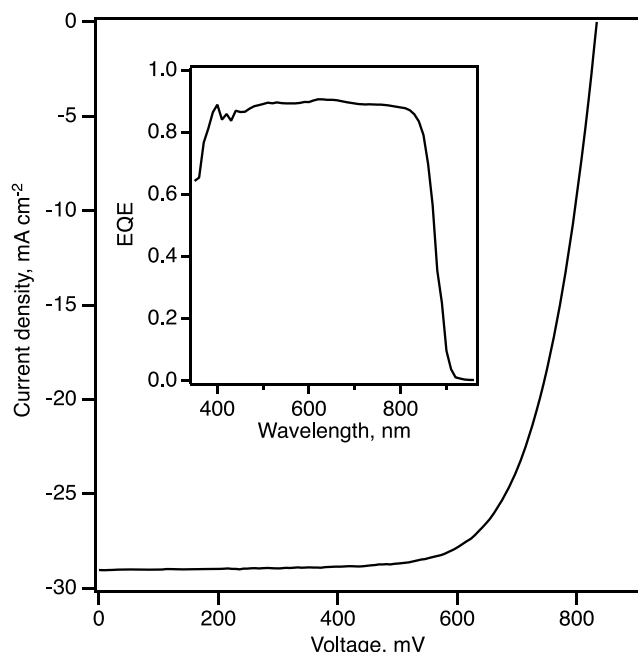


Figure 8. Current density versus applied voltage and EQE (inset) for Cu-doped CdSe/CdTe solar cells.

samples. Chemical imaging showed that heterogeneous Se and Cl distributions modulate bandgap with depth, but also within crystalline grains.^[21,60] In addition, Cu dopants could have heterogeneous distributions in CdTe solar cells.^[76] Despite complex chemical compositions which occurred due to nonequilibrium growth, high-efficiency CdSeTe solar cells can be fabricated using a range of methods and with different Se distributions.

Because recombination velocity $S_{\text{back}} > 10^5 \text{ cm s}^{-1}$ near the back contact,^[77] recombination was near-instant for carriers that diffuse to the back of the solar cell. This led to shortening of the carrier lifetime, and measured lifetime was not representative of the bulk SRH defect density. Kephart et al. investigated metal oxides (Ta_2O_3 , TiO_2 , SiO_2 , and Al_2O_3)

with high resistivity and high-predicted conduction band offset as back-contact passivation layers.^[55] The best passivation was found with Al_2O_3 , where S_{back} was reduced by three orders of magnitude, to $S_{\text{back}} < 200 \text{ cm s}^{-1}$.^[35] Therefore, to reduce the impact of back contact recombination on carrier lifetime analysis, we applied sputtered Al_2O_3 to passivate back contacts for some samples in this study. Alumina is insulating, and passivated samples in this study were used as test structures.

Device Modeling: We used COMSOL to simulate the device band structure during TRPL measurements.^[78] Briefly, COMSOL solved Poisson's equation self-consistently with the time-dependent electron and hole continuity equations. The bands were constructed at each time step using the solution for the electron potential ($V(x, t)$): $E_c(x, t) = -(V(x, t)\chi(x))$ and $E_v(x, t) = -(V(x, t) + \chi(x) + E_g(x))$, where $\chi(x)$ is the electron affinity and $E_g(x)$ is the bandgap. Material and device parameters used in simulations were described.^[79] Specifically, simulations included bandgap grading consistent with experimental data from CL and recombination lifetime changes with depth in the absorber. A manuscript with TRPL modeling code is in preparation.^[36]

Spectroscopy: PL emission spectra were measured with 632.8 nm constant wave (CW) HeNe laser excitation. ERE was determined using integrating sphere and spectrally corrected measurements with a spectrograph and a Si CCD detector.^[24]

For TRPL, regeneratively amplified 1.1 MHz Yb:KGW laser system with optical parametric amplifier (Light Conversion) was used. As shown in Figure 9, for excitation, we use collinear setup with a multimode optical fiber. As measured by scanning knife edge across the excitation beam at the sample position, excitation beam diameter is $60 \mu\text{m}$. For photon counting, we used avalanche photodiodes (PDM APDs, Micro Photon Devices) and PicoHarp300 (Picoquant) time-correlated single photon counting (TCSPC) electronics. Because of the small detector area, APDs were used with multimode optical fibers. PL emission was detected with 10–44 nm bandpass filters with maxima from 820 to 920 nm. Similar lifetimes were measured in this detection range. To avoid photon pileup in TCSPC measurements when injection was changed by several orders of magnitude, neutral density filters in front of detectors were used to maintain photon counting rate at $< 2\%$ of the laser repetition rate.

Time-Resolved Microscopy: To differentiate near-interface and bulk recombination in solar cells, we developed time-resolved microscopy setup for correlative 515 and 1030 nm excitation (Figure 9). Based on different absorption profiles for aforementioned bandgap and sub-band gap excitation, carriers are generated near the interface (one-photon excitation, 1PE, $\lambda_{\text{excitation}} = 515 \text{ nm}$) or uniformly in the thin film (two-photon

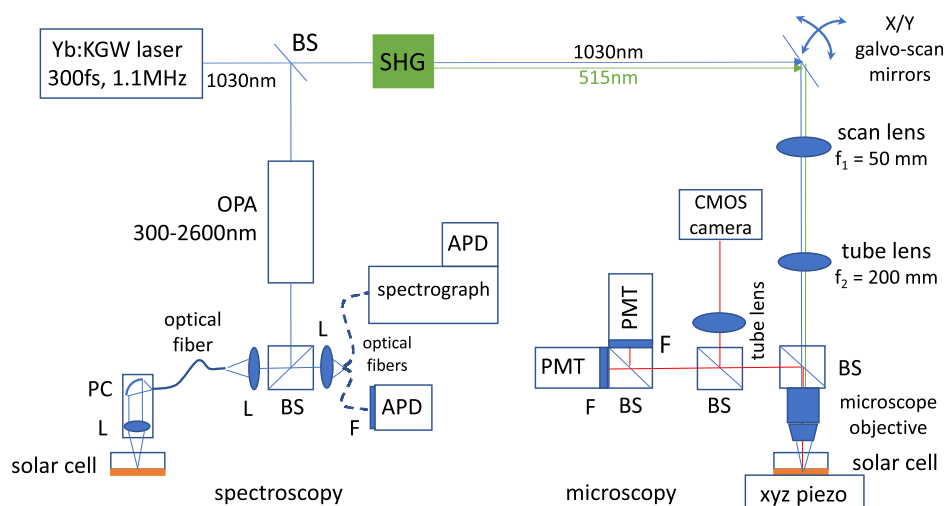


Figure 9. Illustration of time-resolved spectroscopy and microscopy setups. SHG—second harmonics generation, OPA—optical parametric amplifier, BS—dichroic beamsplitter, L—lens, PC—off-axis parabolic collimator, F—bandpass and neutral density filters, APD—avalanche photo diode, PMT—photomultiplier.

excitation, 2PE, $\lambda_{\text{excitation}} = 1030 \text{ nm}$). We modified homebuilt 2PE TRPL microscope described by Motz et al.^[80] to include $f_1 = 50 \text{ mm}$ scan (Thorlabs SL50-CLS2) and $f_2 = 200 \text{ mm}$ tube (Thorlabs TL200-CLS2) lenses designed for imaging at 1030 and 515 nm. In addition to enabling correlative microscopy with near-interface and bulk carrier generation, $f_2/f_1 = 4$ provided for excitation beam expansion, overfilling microscope objective for diffraction-limited imaging and still allowing us use small (10 mm, Cambridge Technology) galvoscan mirrors, which can be scanned at kHz rates.

We used adjustable working distance microscope objective (Zeiss LD Plan-NEOFLUAR 40 \times /0.6) for imaging through glass, which in our case was 2.8 mm-thick glass substrate in solar cells. Video-rate galvanic scanning and imaging with a sCMOS camera (Quantalux, Thorlabs) were used to find region of interest for carrier lifetime microscopy. Time-resolved measurements were taken with hybrid photomultiplier (PMT) detectors (PMA Hybrid 50, Picoquant), sample scanning with piezo xyz stage (PI Nano XYZ), and TSCPC electronics. Integration 0.5 s per pixel at 2% counting rate allows acquisition of 11 000 signal photons per pixel and 50 \times 50-pixel images consisting of 2500 TRPL decays are acquired in about 40 min. Data were analyzed using MATLAB (conversion of TRPL decays to time-resolved image stacks and fitting to exponential decay models) and Fiji/ImageJ (image stack analysis).

Acknowledgements

The authors thank Dmitry Krasikov for critically reading drafts of this manuscript. This material was based upon work supported by the U.S. Department of Energy's Office of Energy Efficiency and Renewable Energy (EERE) under the Solar Technology Office Award Numbers DE-EE0008974 (solar cell fabrication—First Solar) and 34350 (characterization and modeling). This work was authored, in part, by the National Renewable Energy Laboratory, operated by Alliance for Sustainable Energy, LLC, for the U.S. Department of Energy (DOE) under contract no. DE-AC36-08GO28308. The views expressed herein do not necessarily represent the views of the U.S. Department of Energy or the United States Government. This article has been contributed to by US Government contractors and their work is in the public domain in the USA.

Conflict of Interest

The authors declare no conflict of interest.

Data Availability Statement

Research data are not shared.

Keywords

CdTe, characterizations, photoluminescence, solar cells, thin films

Received: December 21, 2020

Revised: February 11, 2021

Published online: March 3, 2021

- [1] N. M. Haegel, R. Margolis, T. Buonassisi, D. Feldman, A. Froitzheim, R. Garabedian, M. Green, S. Glunz, H.-M. M. Henning, B. Holder, I. Kaizuka, B. Kroposki, K. Matsubara, S. Niki, K. Sakurai, R. A. Schindler, W. Tumas, E. R. Weber, G. Wilson, M. Woodhouse, S. Kurtz, *Science* **2017**, 356, 141.
- [2] A. Kanevce, M. O. Reese, T. M. Barnes, S. A. Jensen, W. K. Metzger, *J. Appl. Phys.* **2017**, 121, 214506.

- [3] T. Song, A. Kanevce, J. R. Sites, *J. Appl. Phys.* **2016**, 119, 233104.
- [4] T. Ablekim, E. Colegrove, W. K. Metzger, *ACS Appl. Energy Mater.* **2018**, 1, 5135.
- [5] G. K. Liyanage, A. B. Phillips, F. K. Alfidhili, R. J. Ellingson, M. J. Heben, *ACS Appl. Energy Mater.* **2019**, 2, 5419.
- [6] M. A. Green, Y. Hishikawa, E. D. Dunlop, D. H. Levi, J. Hohl-Ebinger, A. W. Y. Ho-Baillie, *Prog. Photovoltaics Res. Appl.* **2018**, 26, 427.
- [7] <https://www.nrel.gov/pv/module-efficiency.html> (accessed: February 2021).
- [8] J.-F. Guillemoles, T. Kirchartz, D. Cahen, U. Rau, *Nat. Photonics* **2019**, 13, 501.
- [9] M. A. Green, A. W. Y. Ho-Baillie, *ACS Energy Lett.* **2019**, 4, 1639.
- [10] M. D. Mia, C. H. Swartz, S. Paul, S. Sohal, C. R. Grice, Y. Yan, M. Holtz, J. V. Li, *J. Vac. Sci. Technol. B* **2018**, 36, 052904.
- [11] W. K. Metzger, D. Albin, D. Levi, P. Sheldon, X. Li, B. M. Keyes, R. K. Ahrenkiel, *J. Appl. Phys.* **2003**, 94, 3549.
- [12] D. Kuciauskas, P. Dippo, Z. Zhao, L. Cheng, A. Kanevce, W. K. Metzger, M. Gloeckler, *IEEE J. Photovoltaics* **2016**, 6, 313.
- [13] I. L. Repins, B. Egaas, L. M. Mansfield, M. A. Contreras, C. P. Muzzillo, C. Beall, S. Glynn, J. Carapella, D. Kuciauskas, *Rev. Sci. Instrum.* **2015**, 86, 013907.
- [14] E. S. Barnard, B. Ursprung, E. Colegrove, H. R. Moutinho, N. J. Borys, B. E. Hardin, C. H. Peters, W. K. Metzger, P. J. Schuck, *Adv. Mater.* **2017**, 29, 1603801.
- [15] D. Kuciauskas, D. Lu, S. Grover, G. Xiong, M. Gloeckler, *Appl. Phys. Lett.* **2017**, 111, 233902.
- [16] X. Zheng, D. Kuciauskas, J. Moseley, E. Colegrove, D. S. Albin, H. Moutinho, J. N. Duenow, T. Ablekim, S. P. Harvey, A. Ferguson, W. K. Metzger, *APL Mater.* **2019**, 7, 071112.
- [17] D. Kuciauskas, S. Farrell, P. Dippo, J. Moseley, H. Moutinho, J. V. Li, A. M. Allende Motz, A. Kanevce, K. Zaunbrecher, T. A. Gessert, D. H. Levi, W. K. Metzger, E. Colegrove, S. Sivananthan, *J. Appl. Phys.* **2014**, 116, 123108.
- [18] B. Fluegel, K. Alberi, M. J. DiNezza, S. Liu, Y.-H. Zhang, A. Mascarenhas, *Phys. Rev. Appl.* **2014**, 2, 034010.
- [19] B. Gaury, P. M. Haney, *J. Appl. Phys.* **2016**, 119, 125105.
- [20] D. Kuciauskas, T. H. Myers, T. M. Barnes, S. A. Jensen, A. M. Allende Motz, *Appl. Phys. Lett.* **2017**, 110, 083905.
- [21] T. A. M. Fiducia, B. G. Mendis, K. Li, C. R. M. Grovenor, A. H. Munshi, K. Barth, W. S. Sampath, L. D. Wright, A. Abbas, J. W. Bowers, J. M. Walls, *Nat. Energy* **2019**, 4, 504.
- [22] J. Guo, A. Mannodi-Kanakkithodi, F. G. Sen, E. Schwenker, E. S. Barnard, A. Munshi, W. Sampath, M. K. Y. Chan, R. F. Klie, *Appl. Phys. Lett.* **2019**, 115, 153901.
- [23] V. Sarritzu, N. Sestu, D. Marongiu, X. Chang, S. Masi, A. Rizzo, S. Colella, F. Quochi, M. Saba, A. Mura, G. Bongiovanni, *Sci. Rep.* **2017**, 7, 44629.
- [24] D. Kuciauskas, J. Moseley, P. Ščajevo, D. Albin, *Phys. Status Solidi* **2020**, 14, 1900606.
- [25] W. K. Metzger, S. Grover, D. Lu, E. Colegrove, J. Moseley, C. L. Perkins, X. Li, R. Mallick, W. Zhang, R. Malik, J. Kephart, C.-S. Jiang, D. Kuciauskas, D. S. Albin, M. M. Al-Jassim, G. Xiong, M. Gloeckler, *Nat. Energy* **2019**, 4, 837.
- [26] W. Metzger, R. Ahrenkiel, J. Dashdori, D. Friedman, *Phys. Rev. B* **2005**, 71, 035301.
- [27] A. Kanevce, D. H. Levi, D. Kuciauskas, *Prog. Photovoltaics Res. Appl.* **2014**, 22, 1138.
- [28] A. Kanevce, D. Kuciauskas, D. H. Levi, A. M. Allende Motz, S. W. Johnston, *J. Appl. Phys.* **2015**, 118, 045709.
- [29] D. Kuciauskas, A. Kanevce, J. N. Duenow, P. Dippo, M. Young, J. V. Li, D. H. Levi, T. A. Gessert, *Appl. Phys. Lett.* **2013**, 102, 173902.
- [30] M. Maiberg, R. Scheer, *J. Appl. Phys.* **2014**, 116, 123711.

- [31] T. P. Weiss, B. Bissig, T. Feurer, R. Carron, S. Buecheler, A. N. Tiwari, *Sci. Rep.* **2019**, 9, 5385.
- [32] J. Moseley, D. Krasikov, D. Kuciauskas, in *2020 IEEE 47th Photovolt. Spec. Conf.*, IEEE, Piscataway, NJ, USA **2020**, p. 2062–2065.
- [33] P. Ščajev, S. Miasojedovas, A. Mekys, D. Kuciauskas, K. G. Lynn, S. K. Swain, K. Jarašiūnas, *J. Appl. Phys.* **2018**, 123, 025704.
- [34] C. H. Swartz, M. Edirisooriya, E. G. LeBlanc, O. C. Noriega, P. A. R. D. Jayathilaka, O. S. Ogedengbe, B. L. Hancock, M. Holtz, T. H. Myers, K. N. Zaunbrecher, *Appl. Phys. Lett.* **2014**, 105, 222107.
- [35] D. Kuciauskas, J. M. Kephart, J. Moseley, W. K. Metzger, W. S. Sampath, P. Dippo, *Appl. Phys. Lett.* **2018**, 112, 263901.
- [36] J. Moseley, in preparation.
- [37] J. Moseley, H. L. Guthrey, M. Al-Jassim, W. K. Metzger, *Physics, Simulation, Photonic Eng. Photovolt. Devices VIII* (Eds: A. Freundlich, M. Sugiyama, L. Lombez), SPIE, Piscataway, NJ, USA **2019**, p. 34.
- [38] A. Kanevce, J. Moseley, M. Al-Jassim, W. K. Metzger, *IEEE J. Photovoltaics* **2015**, 5, 1722.
- [39] J. Moseley, W. K. Metzger, H. R. Moutinho, N. Paudel, H. L. Guthrey, Y. Yan, R. K. Ahrenkiel, M. M. Al-Jassim, *J. Appl. Phys.* **2015**, 118, 025702.
- [40] M. Gloeckler, I. Sankin, Z. Zhao, *IEEE J. Photovoltaics* **2013**, 3, 1389.
- [41] J. Perrenoud, L. Kranz, C. Gretener, F. Pianezzi, S. Nishiwaki, S. Buecheler, A. N. Tiwari, *J. Appl. Phys.* **2013**, 114, 174505.
- [42] J. Yang, W. K. Metzger, S. Wei, *Appl. Phys. Lett.* **2017**, 111, 042106.
- [43] D. Kuciauskas, P. Dippo, A. Kanevce, Z. Zhao, L. Cheng, A. Los, M. Gloeckler, W. K. Metzger, *Appl. Phys. Lett.* **2015**, 107, 243906.
- [44] W. Tress, *Adv. Energy Mater.* **2017**, 7, 1602358.
- [45] M. Stollerfoht, C. M. Wolff, J. A. Márquez, S. Zhang, C. J. Hages, D. Rothhardt, S. Albrecht, P. L. Burn, P. Meredith, T. Unold, D. Neher, *Nat. Energy* **2018**, 3, 847.
- [46] J. Yang, W. Yin, J. Park, J. Ma, S. Wei, *Semicond. Sci. Technol.* **2016**, 31, 083002.
- [47] E. Yablonovitch, T. J. Gmitter, R. Bhat, *Phys. Rev. Lett.* **1988**, 61, 2546.
- [48] W. K. Metzger, M. Gloeckler, *J. Appl. Phys.* **2005**, 98, 063701.
- [49] J. D. Major, *Semicond. Sci. Technol.* **2016**, 31, 093001.
- [50] B. G. Mendis, D. Gachet, J. D. Major, K. Durose, *Phys. Rev. Lett.* **2015**, 115, 218701.
- [51] B. Gaury, P. M. Haney, *J. Appl. Phys.* **2016**, 120, 234503.
- [52] B. Gaury, P. M. Haney, *Phys. Rev. Appl.* **2017**, 8, 054026.
- [53] B. Gaury, P. M. Haney, *ACS Appl. Energy Mater.* **2019**, 2, 144.
- [54] T. A. M. Fiducia, K. Li, A. H. Munshi, K. Barth, W. S. Sampath, C. R. M. Grovenor, J. M. Walls, *IEEE J. Photovoltaics* **2020**, 10, 685.
- [55] J. M. Kephart, A. Kindvall, D. Williams, D. Kuciauskas, P. Dippo, A. Munshi, W. S. Sampath, *IEEE J. Photovoltaics* **2018**, 8, 587.
- [56] M. J. Watts, T. A. M. Fiducia, B. Sanyal, R. Smith, J. M. Walls, P. Goddard, *J. Phys. Condens. Matter* **2020**, 32, 125702.
- [57] D. N. Krasikov, A. V. Scherbinin, A. A. Knizhnik, A. N. Vasiliev, B. V. Potapkin, T. J. Sommerer, *J. Appl. Phys.* **2016**, 119, 085706.
- [58] J.-H. Yang, L. Shi, L.-W. Wang, S.-H. Wei, *Sci. Rep.* **2016**, 6, 21712.
- [59] J. Yang, S.-H. Wei, *Chin. Phys. B* **2019**, 28, 086106.
- [60] T. A. M. Fiducia, K. Li, A. H. Munshi, K. Barth, W. S. Sampath, C. R. M. Grovenor, J. M. Walls, *IEEE J. Photovoltaics* **2020**, 10, 685.
- [61] I. Sankin, D. Krasikov, *Phys. Status Solidi A* **2019**, 216, 1800887.
- [62] D. Krasikov, I. Sankin, *J. Mater. Chem. A* **2017**, 5, 3503.
- [63] K. N. Zaunbrecher, D. Kuciauskas, C. H. Swartz, P. Dippo, M. Edirisooriya, O. S. Ogedengbe, S. Sohal, B. L. Hancock, E. G. LeBlanc, P. A. R. D. Jayathilaka, T. M. Barnes, T. H. Myers, *Appl. Phys. Lett.* **2016**, 109, 091904.
- [64] D. Kuciauskas, K. Wernsing, S. A. Jensen, T. M. Barnes, T. H. Myers, R. A. Bartels, *IEEE J. Photovoltaics* **2016**, 6, 1581.
- [65] C. R. M. Grovenor, *J. Phys. C Solid State Phys.* **1985**, 18, 4079.
- [66] V. Consonni, N. Baier, O. Robach, C. Cayron, F. Donatini, G. Feuillet, *Phys. Rev. B* **2014**, 89, 035310.
- [67] C.-S. Jiang, H. R. Moutinho, J. Moseley, A. Kanevce, J. N. Duenow, E. Colegrove, C. Xiao, W. K. Metzger, M. M. Al-Jassim, in *Proc. 44th IEEE Photovoltaic Specialist Conf.*, IEEE, Piscataway, NJ, USA **2017**, pp. 1312–1316.
- [68] C. Xiao, C.-S. Jiang, K. Blaine, M. Amarasinghe, E. Colegrove, W. K. Metzger, M. M. Al-Jassim, N. M. Haegel, H. Moutinho, *Cell Rep. Phys. Sci.* **2020**, 1, 100230.
- [69] M. Tuteja, P. Koirala, V. Palekis, S. MacLaren, C. S. Ferekides, R. W. Collins, A. A. Rockett, *J. Phys. Chem. C* **2016**, 120, 7020.
- [70] Y. Jin, S. T. Dunham, *IEEE J. Photovoltaics* **2017**, 7, 329.
- [71] M. Krause, A. Nikolaeva, M. Maiberg, P. Jackson, D. Hariskos, W. Witte, J. A. Márquez, S. Levchenko, T. Unold, R. Scheer, D. Abou-Ras, *Nat. Commun.* **2020**, 11, 4189.
- [72] S. Misra, J. A. Aguiar, S. Gardner, X. Sang, R. R. Unocic, A. Munshi, W. S. Sampath, C. S. Ferekides, M. A. Scarpulla, *ACS Appl. Energy Mater.* **2020**, 3, 1749.
- [73] A. Danielson, A. Abbas, J. M. Walls, Z. Holman, W. Sampath, A. Munshi, A. Onno, W. Weigand, A. Kindvall, C. Reich, Z. J. Yu, J. Shi, D. Kuciauskas, in *2019 IEEE 46th Photovoltaics Specialists Conf.*, IEEE, Piscataway, NJ, USA **2019**, pp. 3018–3023.
- [74] B. E. McCandless, W. A. Buchanan, C. P. Thompson, G. Sriramagiri, R. J. Lovelett, J. Duenow, D. Albin, S. Jensen, E. Colegrove, J. Moseley, H. Moutinho, S. Harvey, M. Al-Jassim, W. K. Metzger, *Sci. Rep.* **2018**, 8, 14519.
- [75] T. Ablekim, J. N. Duenow, X. Zheng, H. Moutinho, J. Moseley, C. L. Perkins, S. W. Johnston, P. O'Keefe, E. Colegrove, D. S. Albin, M. O. Reese, W. K. Metzger, *ACS Energy Lett.* **2020**, 5, 892.
- [76] D. Mao, G. Blatz, C. E. Wickersham, M. Gloeckler, *Sol. Energy Mater. Sol. Cells* **2016**, 157, 65.
- [77] D. Kuciauskas, A. Kanevce, J. M. Burst, J. N. Duenow, R. Dhere, D. S. Albin, D. H. Levi, R. K. Ahrenkiel, *IEEE J. Photovoltaics* **2013**, 3, 1319.
- [78] J. Moseley, S. Grover, D. Lu, G. Xiong, H. L. Guthrey, M. M. Al-Jassim, W. K. Metzger, *J. Appl. Phys.* **2020**, 128, 103105.
- [79] J. Moseley, D. Krasikov, D. Kuciauskas, in *2020 IEEE 47th Photovoltaics Specialists Conf.*, IEEE, Piscataway, NJ, USA **2020**, pp. 2062–2065.
- [80] A. A. Motz, J. Squier, D. Kuciauskas, S. Johnston, A. Kanevce, D. Levi, in *2015 IEEE 42nd Photovoltaics Specialists Conf.*, IEEE, Piscataway, NJ, USA **2015**, pp. 1–6.